Heat-resistant coatings based on high-entropy alloy (MoTaNbZrHf)SiB with increased silicon content obtained by magnetron sputtering method

F.V. Kiryukhantsev-Korneev, A.D. Chertova, N.V. Shvyndina, E.A. Levashov

University of Science and Technology 'MISIS', 119049, Moscow, Leninsky Prospekt, 4c1

Received October 07, 2023

Revised

Accepted

In the present work, magnetron sputtering of (MoTaNbZrHf)SiB and SiBC targets yielded: single-layer (MoTaNbZrHf)-Si-B, double- and multilayer (MoTaNbZrHf)-Si-B/Si-B-C, and nanocomposite coatings (MoTaNbZrHf)-Si-B-C. Special attention was paid to investigate the effect of increased silicon content on the structure and heat resistance of the developed coatings. The results showed that the single-layer and nanocomposite coatings have a homogeneous structure with a uniform distribution of elements over the thickness. The bi- and multilayer coatings contained (MoTaNbZrHf)-Si-B/Si-B-C layers with thicknesses of 9.1/3.9 and 1.7/0.6 μm, respectively. The introduction of additional silicon-containing phases into the (MoTaNbZrHf)-Si-B coatings resulted in a decrease in the specific mass change from -3.1 to 0.15-0.20 mg/cm^2 at 1000ºC. Annealing at 1500ºC showed that the (MoTaNbZrHf)-Si-B/Si-B-C bilayer coatings possess a minimum oxide layer thickness of 9.2 μm and a specific mass loss of 0.95 mg/cm^2, which is 1.5 and 1.8 times lower than the values obtained for the (MoTaNbZrHf)-Si-B single-layer

coating. At 1600ºC, the (MoTaNbZrHf)-Si-B single-layer coatings were completely oxidised, while the (MoTaNbZrHf)-Si-B/Si-B-C bi- and multilayer coatings were fragmentarily preserved, which is related to the high silicon content in their composition.
DOI: 10.31857/S00441856250106e6

Introduction

In materials science, increased attention is currently being paid to the study of high-entropy alloys (HEAs), which are alloys composed of 5 to 10 or more elements in approximately equiatomic or equimolar ratios [1-8]. These alloys are interesting due to their unique properties resulting from four effects related to high entropy, crystal lattice distortions, slowed diffusion of alloy components, and the "cocktail" (synergistic) effect [9]. Compared to simple systems, HEAs demonstrate enhanced mechanical characteristics such as: hardness, compressive strength [10], high wear and corrosion resistance [11,12], oxidation resistance and thermal stability [13,14], high saturation magnetization and low coercive force

Among common HEA groups, materials are distinguished based on a) 3d transition metals (Fe, Co, Cr, Ni, Mn, Al, Ti, Cu, V), for example, the Cantor alloy [18], b) 4f transition metals (Gd, Dy, Lu, Tm, Tb, Y) [19], c) low-melting alloys (Al, Ti, Mg, Li, Be) [20], d) refractory metals (Ta, Nb, Zr, Hf, W, V, Ti, Cr) [21,22], and others. Modern research is increasingly devoted to the development of ceramic (bulk) materials in which HEAs play the role of metal. Oxide [23], carbide [24], nitride [25], and less commonly - boride [26] systems based on HEAs are known. Data on HEA silicides is currently very limited. Around 2020, the first results appeared on creating materials based on HEA silicides (MoNbTaTiW)Si_2 [27], (NbMoTaWV)Si_2 [28], (MoWCrTaNb)Si_2 [29], (MoWReCrV)Si_2 [30]. Both small additions of Si (2-17 at.%) [31,32] to HEAs and silicide systems with a stoichiometric ratio of

Si/HEA=2 [27-30,33] are being studied. A promising direction is the creation of heat-resistant ceramics of the HEA-Si-B type, which could replace materials of the Mo-Si-B system, whose ultimate properties have already been achieved [34].

Previously in our laboratory, coatings of (MoTaNbZrHf)-Si-B were obtained using SHS cathodes, having hardness up to 14 GPa, elastic recovery of 39%, good tribological properties, and heat resistance up to 1500°C [35]. This study aims to improve the heat resistance of these coatings.

It is known that increasing the silicon content in coatings enhances their resistance to high-temperature oxidation, which was previously demonstrated in the case of TiBSiN [36], MoSiBN [37], and ZrMoSiB [38] systems. The improvement in heat resistance in this case is associated with the formation of dense protective oxide layers based on Si-O on the coating surface, which prevent further diffusion of oxygen into the mate rial.

Another method to improve the heat resistance of coatings is the formation of multilayer structures containing additional layers of Si or its compounds (SiC, SiCN, Si_3N_4) in addition to layers of the main material. Known multilayer coatings, such as ZrB_2/SiC [39], are resistant to oxidation for more than 300 hours at 900 ^{0}C and 217 hours at 1500 ^{0}C. In [40], BCx/SiC multilayer coatings with high heat resistance up to 1200°C were fabricated by magnetron sputtering, while single-layer BCx completely oxidized at just 700°C. The mechanism for improving the heat resistance of coatings when adding silicon-containing layers is the same as when doping them with silicon. The introduction of additional silicon-containing layers allows increasing the thermal stability and heat resistance of coatings, which was previously demonstrated by us in the study of multilayer coatings ZrSiB/SiBC [41], MoSiB/SiBC [42], TiAlSiCN/SiBCN [43]. In the present work, previously obtained coatings in the Si-B-C-(N) system [44] were chosen as the silicon-containing layer,

characterized by hardness up to 20 GPa, elastic recovery up to 53%, as well as heat resistance above 1200°C.

The purpose of this work is to study the structure and determine the heat resistance of coatings with increased silicon content, obtained by magnetron sputtering of (MoTaNbZrHf)SiB and SiBC targets. Four types of coatings were investigated: single-layer (SL) with the basic composition (MoTaNbZrHf)-Si-B, double-layer (DL) applied by sequential sputtering of targets, multilayer (ML) applied by cyclically repeated sputtering of targets, and nanocomposite (NC) applied by simultaneous sputtering of targets.

Experimental methodology

The magnetron sputtering target (Ø120x10 mm) was manufactured by combining methods of mechanical alloying, self-propagating high-temperature synthesis (SHS), and hot pressing (HP). To obtain powder granules of solid solution, mechanical alloying (MA) of a mixture of metal powders Mo (PM-99.95), Nb (NbP-3a), Hf (GFM-2), Ta (TaPM), and Zr (PTsrK-1) with an equiatomic ratio of components was carried out in a planetary centrifugal mill "Activator-2SL" (LLC "Chemical Engineering Plant", Russia). The process was conducted in sealed stainless steel drums in an Ar environment at a rotation speed of 700 rpm, with a mass ratio of mixture components to grinding bodies of 1:15 and a time of 30 min. Further, in the same mill under similar conditions, reaction mixtures of the obtained granules with powders were prepared: 60 at.% Si (less than 63 μm) and 5 at.% B (B-99A). SHS was conducted in Ar (99.9995%). The synthesis products were ground in a rotating ball mill using carbide linings and grinding bodies for 8 hours. HP was performed on a DSP-515 SA unit (Dr. Fritsch Sondermaschinen GmbH, Germany) in a graphite press mold with a diameter of 120 mm at a temperature of 1300 ° C,

pressure of 35 MPa, and a time of 10 min. The second target SiBC (70%Si-25%B-5%C) with a diameter of 120 mm and a thickness of 10 mm was obtained by hot pressing technology on a DSP-515 SA unit ("Dr. Fritsch", Germany) [44].

The coatings were deposited on a UVN-2M type installation equipped with a disk magnetron and a gas ion source [45]. Substrates in the form of Ø30 mm disks (nickel alloy KhN65VMTYu) and rectangular substrates (polycrystalline aluminum oxide VK-100-1, single-crystal silicon KDB (111)) were used. Deposition on different substrates was carried out in a single technological cycle. Before coating, metal substrates were ground and polished on a Struers Rotopol automatic machine. Ultrasonic cleaning was performed on a UZDN-2T unit in isopropyl alcohol medium for 5 minutes. Immediately before coating, the substrate surface was subjected to ion cleaning using an ion source (voltage was 2.5 kV, current 60 mA, cleaning time 40 min). Deposition of coatings in direct current mode was implemented using a two-channel power supply with an arc suppression system, Pinnacle Plus 5×5 (Advanced Energy). The power supplied to the (MoTaNbZrHf)SiB target was 1 kW, and to SiBC 500 W. The pressure and flow rate of Ar (99.9995%) were 0.1-0.2 Pa and 37.5 ml/min, respectively. The spraying distance of the (MoTaNbZrHf)-Si-B and Si-B-C layers was fixed at 10 and 8 cm, respectively. The distance and power when sputtering the SiBC target were determined by its relatively low electrical conductivity and reduced sputtering rate. When applying double-layer coatings (DL), the duration of substrate positioning sequentially over each of the magnetrons was 1 hour, with a total deposition time of 2 hours. For multilayer coatings (ML), the total deposition time was also 2 hours, the time of cyclic positioning of substrates over each of the magnetrons was 10 minutes, with 6 cycles. Nanocomposite coatings (NC) were deposited for 1 hour with the substrates positioned between the magnetrons.

The chemical composition of the coatings was determined by glow discharge optical emission spectroscopy (GDOES) using a Profiler 2 instrument (Horiba Jobin

Yvon, France) [46]. The structure was studied by scanning electron microscopy (SEM) on an S-3400 instrument (Hitachi, Japan) equipped with a Noran 7 Thermo energy-dispersive spectrometer (EDS). X-ray phase analysis (XRD) was performed on a Phaser D2 instrument (Bruker, USA) using CuKα radiation. To study the oxidation kinetics of the coatings, isothermal annealing was carried out in a SNOL 7.2/1200 furnace at a temperature of 1000°C with holding times of 10, 30, 60, and 180 minutes. Samples in individual alumina crucibles were placed in a furnace preheated to the set temperature. After the holding time elapsed, the samples were removed and cooled to room temperature in air, and photographs of the samples were taken. The values of specific mass change Δm/S (Δm - mass change, S - sample area) of the coatings were calculated depending on the holding time. To study the heat resistance of (MoTaNbZrHf)-Si-B coatings at higher temperatures, non-isothermal (heating and cooling of samples together with the furnace) annealing was carried out in a muffle furnace TK 15.1800.DM.1F manufactured by LLC "Termokeramika" (Russia) at temperatures of 1500°C and 1600°C, with a holding time of 10 minutes at each temperature. The samples were heated at a rate of 5 degrees/min. The structure of the coatings after testing was studied by SEM, EDS, and XRD methods.

Results and discussion

Figure 1 shows SEM micrographs of coating fractures. According to SEM data, the single-layer (SL) coating (MoTaNbZrHf)-Si-B had a thickness of 12.0 μm. For the double-layer coating (DL), the thicknesses of the (MoTaNbZrHf)-Si-B and Si-B-C layers were 9.1 and 3.9 μm, respectively. The lighter layer in the micrograph corresponds to (MoTaNbZrHf)-Si-B, the darker one to Si-B-C. The total thickness of the multilayer coating (ML) was 13.9 μm, with the thicknesses of individual

(MoTaNbZrHf)-Si-B and Si-B-C layers being 1.7 and 0.6 μm, respectively. In the case of the NC coating, the reduction in thickness to 6.7 μm is explained by the increased deposition distance when the substrate table was positioned between the magnetrons. According to SEM studies, all samples were characterized by a dense low-defect structure with no pronounced grain boundaries. The suppression of columnar structure formation favorably distinguishes the obtained coatings from known two- and three-component ion-plasma coatings, in which reactive diffusion of oxygen atoms along grain boundaries typically leads to catastrophic oxidation during high-temperature heating in air [47,48].

The XRD results of the coatings are presented in Figure 1e. In addition to narrow reflections corresponding to the Al_2O_3 substrate, the diffractograms show halos at 2Θ positions: ~27°, ~40°, and ~62°, typical for amorphous coatings. Thus, due to the competitive growth of various silicide phases during coating formation, the introduction of several amorphizing elements (Si and B) simultaneously [49,50], as well as the interruption of crystallite growth during layer-by-layer deposition [51], all coatings had an amorphous structure. Minor differences in diffractogram intensity are explained by different coating thicknesses. XRD studies performed on coatings on metal substrates also confirmed the amorphous structure of the coatings.

Typical elemental profiles of the coatings are presented in Fig. 2. OESTR method studies showed that the SL coating contains, at.%: 51 Si, 7 B, 7 Zr, 7 Nb, 8 Mo, 10 Ta, 10 Nb. Minor impurities of oxygen and iron were detected in the coatings. Metallic impurities can be explained by the abrasion of milling bodies material during the preparation of the sputtering target [52,53]. All elements were uniformly distributed throughout the thickness of the coatings. The lower layer in the double-layer DL coating had a similar composition. The upper layer of the DL coating contained, at.%: 78 Si, 13 B, 9 C. Thus, an increased concentration of silicon was achieved on the surface of the DL coating. The layers in ML coatings had a

composition similar to the composition of the corresponding layers in DL coatings. NC coatings had the following composition, at.%: 61 Si, 12 B, 9 C, 3 Zr, 3 Nb, 3 Mo, 4 Ta, 5 Hf. Compared to the base SL coating, there was an increase in silicon concentration by 10 at.% and boron by 5 at.% with an overall decrease in metal concentrations.

The results of isothermal annealing at 1000°C showed that for the SL coating, there was a sharp decrease in Δm/S to -3.1 mg/cm ^{2} after exposure for 10 min (Fig. 3a), which is associated with coating delamination (Fig. 3b) due to its low adhesion strength and crack resistance, as well as possible structural transformations accompanied by changes in the volume of phase components [45]. In the case of DL, ML, NC coatings, the appearance of the samples after different exposure times changed insignificantly; pronounced delaminations, blistering, cracks, and other defects on the surface were not noticeably observed. The patterns of change in the Δm/S parameter versus exposure time for DL, ML, NC coatings were similar (Fig. 3a). The increase in Δm/S to 0.15-0.21 mg/cm ^{2} within 10 min is associated with the formation of a dense protective oxide film on the surface of these coatings. During subsequent heating and exposure, this film prevents intensive oxidation of the coatings. During exposures ranging from 60 to 180 min, the parameter either decreased (ML, DL) or remained stable (NC).

Figure 4 shows SEM micrographs of the coating surfaces after annealing at 1500°C with a holding time of 10 minutes. On the surface of SL, DL, ML, NC coatings, a layer forms consisting predominantly of borosilicate glass Si:B:O (gray areas without pronounced structural features in SEM images). The area occupied by this phase noticeably increases when transitioning from SL to DL, ML, NC, which confirms the validity of the assumption linking the protective properties of the surface oxide with the silicon concentration in the coatings. The a-Si:B:O layers contain grains of crystalline oxygen-containing phases: (Hf,Zr)SiOx (SL, DL, ML

coatings), (Ta,Hf,Zr)SiOx and HfSiOx (NC coatings). The sizes of individual grains and their agglomerates of these phases decrease from 5-20 μm to 0.5-4.5 μm when transitioning from SL to DL, ML, NC coatings.

SEM images of cross-sectional fractures and EDS maps of elemental distribution for SL, DL, ML and NC coatings after annealing at 1500°C are presented in Figure 5. On the surface of the SL coating, a protective film based on a-Si:B:O formed, containing predominantly (Hf,Zr,Nb,Ta)SiOx crystallites with sizes of 0.6-1.6 μm in the near-surface layer and (Hf,Zr)SiOx crystallites with sizes of 100-500 nm inside the film. For the DL coating, the formation of a protective film based on a-Si:B:O with (Hf,Zr)SiOx particles of 0.2-1.2 μm in size was observed, located on the sample surface and at the "protective film-non-oxidized coating" interface. The film formed during the annealing process on the surface of the ML coating consisted of several layers: a) an upper layer based on a-Si:B:O with locally positioned (Hf,Zr)SiOx crystallites of 150-700 nm in size; b) a middle layer containing larger (Hf,Zr)SiOx particles ranging from 0.8 to 1.7 μm; c) a lower layer consisting of a-Si:B:O+(Hf,Zr)SiOx. On the surface of the NC coating, a protective film formed, consisting of an amorphous a-Si:B:O matrix and (Ta,Hf,Zr)SiOx crystallites ranging from 0.2 to 2.0 μm in size.

The thicknesses of protective films for SL, DL, ML, and NC coatings, annealed at 1500°C, were 13.3, 9.2, 12.7, and 10.7 μm (Fig.6a), respectively. The specific mass change of coatings (Fig.6b) and the difference between the thickness of the original coating and the thickness of the unoxidized layer, characterizing the degree of coating burnout (mass loss) during annealing (Fig.6a), were also determined. The DL coating was characterized by the minimum thickness of the oxygen-containing layer and mass loss. This fact may be related to the large thickness of the upper SiBC layer, which is characterized by an increased silicon content, which in turn accelerates the formation of a protective Si:B:O layer on the surface.

Thus, annealing in air at 1500°C showed that there is a correlation between the surface area of annealed coatings occupied by the Si:B:O phase and their protective properties. An increase in the Si:B:O area, as well as a decrease in the size of crystallites of oxygen-containing phases, lead to an increase in the heat resistance of coatings.

Figure 7 shows SEM micrographs of the coating surface after annealing at a temperature of 1600°C with a holding time of 10 minutes. On the surface of SL, DL, ML, NC coatings, a layer is formed consisting of borosilicate glass Si:B:O and grains of crystalline oxygen-containing phases: (Hf,Zr,Nb,Ta)SiOx (SL and NC coatings), (Hf,Zr)SiOx (DL and ML coatings). For all coatings, the grains of oxygen-containing phases have predominantly dendritic form. Moreover, the minimum particle size of 0.5-5.0 μm is observed for the ML coating.

SEM images of cross-sectional fractures and EDS maps of element distribution in SL, DL, ML, and NC coatings after annealing at 1600 ºC are presented in Fig. 8. The SL coating was completely oxidized during the annealing process, forming a 90 μm thick layer based on a-Si:B:O with (Hf,Zr,Nb,Ta)SiOx particles. When studying the cross-sectional fracture of the DL coating, 90% of the examined sample area corresponded to complete oxidation of the coating with the formation of a 60 μm thick a-Si:B:O+(Hf,Zr)SiOx layer. In 10% of the examined area, segments of non-oxidized DL coating with a thickness of 12 μm were detected (Fig. 8b). The increase in the thickness of the non-oxidized coating layer with increasing annealing temperature may be associated with changes in the volume of phase components resulting from structural transformations [54]. The thickness of the oxygen-containing layer for the DL coating was 13 μm. In the case of the ML coating, areas of preserved non-oxidized coating occupied 25% of the examined fracture surface area (Fig. 8c). The composition and structure of the protective film were identical to the data obtained at 1500 ºC. The thicknesses of the protective film and the non-

oxidized layer for the ML coating were 17 and 13 μm, respectively. The NC coating was preserved fragmentarily (Fig. 8.g). The preserved coating areas were surrounded by an oxygen-containing film based on Si:B:O.

According to XRD data, for all coatings after annealing at a temperature of 1500 °C, the formation of the following phases is observed: silicides t-Ta_5Si_3 (ICDD 82-9452) and h-Zr_5Si_3 (ICDD 79-4988), corresponding to the non-oxidized layer of the coating, as well as hafnium silicate t-$HfSiO_4$ (ICDD 77-1759), oxides o-Ta_2O_5 (ICDD 25-0922) and m-HfO_2 (ICDD 34-0104), related to the protective film (Fig. 9a). Also, the formation of oxide m-ZrO_2 cannot be excluded, as its line positions coincide with the peak positions of m-HfO_2. For SL, DL, and NC coatings, the peaks with maximum intensity corresponded to the t-$HfSiO_4$ phase, while for the ML coating, the peaks of m-HfO_2 had the maximum intensity. The main peaks of t-$HfSiO_4$ were detected at positions 2Θ = 20.1°, 27.2°, 35.7°, 47.6°. The crystallite sizes of this phase, determined by the Debye-Scherrer formula for the non-overlapping peak at 2Θ = 20.1°, were ~50 nm for SL and NC coatings and ~30 nm for DL and ML coatings. It should be noted that for the ML coating, the amorphous halo observed in the initial state was preserved after annealing at 1500°C.

X-ray diffraction patterns of coatings annealed at 1600°C are presented in Fig. 9b. The formation of new oxide phases was observed: h-MoO_3 (ICDD 77-1759) (SL, DL, ML, NC), m-Nb_2O_5 (ICDD 68-0148) (SL), t-NbO_2 (ICDD 74-2387) (DL, ML, NC). It is worth noting the absence of peaks from t-Ta_5Si_3 and h-Zr_5Si_3 phases for SL and DL coatings, which is associated with their significant oxidation (Fig.8a,b). For the ML coating, an increase in the intensity of the t-$HfSiO_4$ phase peaks was observed compared to annealing at 1500°C. Peaks from silicides t-Ta_5Si_3 and h-Zr_5Si_3, corresponding to the non-oxidized coating layer, were preserved, but their intensity decreased by ~2.5 times compared to 1500°C. For the NC sample, the

overall peak intensity decreased by 5 times, while low-intensity peaks from the t-Ta_5Si_3 and h-Zr_5Si_3 phases were detected.

Thus, annealing in air at 1600°C showed that the ML coating has the best oxidation resistance. A similar positive effect from using silicon-containing phase layers in the coating architecture was observed in works [43,55], dedicated to the study of TiAlSiCN/SiBCN coatings. The high diffusion-barrier characteristics of SiBCN layers provided increased heat resistance by suppressing the diffusion of components to the surface from the main composition layers, TiAlSiCN.

Conclusions

Single-layer (SL) coatings of (MoTaNbZrHf)-Si-B, as well as single- (NC), double- (DL), and multi-layer (ML) coatings with increased silicon concentration were obtained by magnetron sputtering, deposited by sequential or simultaneous sputtering of (MoTaNbZrHf)SiB and SiBC targets.

The SL and NC coatings, with thicknesses of 12.0 and 6.7 μm, were characterized by a homogeneous structure and uniform distribution of elements throughout the thickness. For the double-layer coating, the thicknesses of (MoTaNbZrHf)-Si-B and Si-B-C layers were 9.1 and 3.9 μm, respectively. The multi-layer coating with a thickness of 13.9 μm consisted of individual (MoTaNbZrHf)-Si-B and Si-B-C layers with thicknesses of 1.7 and 0.6 μm, respectively.

The results of isothermal annealing showed that DL, ML, and NC coatings obtained using the SiBC target are characterized by a minimum specific mass change $\Delta m/S = 0.15\text{-}0.21$ mg/cm^2 and in terms of oxidation resistance at 1000°C outperform the single-layer SL coatings having $\Delta m/S = -3.1$ mg/cm^2.

Non-isothermal annealing showed that all coatings maintain their protective properties at 1500°C. The specific mass change of the coatings decreased by 1.2-2.0 times when transitioning from the single-layer SL coating to DL, ML, and NC coatings. At 1600°C, the SL and NC coatings were completely oxidized, while the DL and ML coatings were partially preserved, which is associated with the positive effect of the SiBC additive, characterized by an increased silicon content.

Acknowledgment

This work was financially supported by the Ministry of Science and Higher Education of the Russian Federation within the framework of the state assignment (project No. 0718-2020-0034).

REFERENCES

1. Ren J., Zhang Y., Zhao D., Chen Y., Guan S., Liu Y., et al. // *Nature.* 2022. Vol. 608. P. 62–68. DOI: 10.1038/s41586-022-04914-8
2. Pan Q., Zhang L., Feng R., Lu Q., An K., Chuang A.C., et al. // *Science* . 2021. Vol. 374. P. 984–989.
3. George E.P., Raabe D., Ritchie R.O. // *Nature Reviews Materials.* 2019. Vol. 4. P. 515–534. DOI: 10.1038/s41578-019-0121-4
4. Tsai M.H., Yeh J.W. // *Materials Research Letters.* 2014. Vol. 2. P. 107–123. DOI: 10.1080/21663831.2014.912690
5. Li J., Huang Y., Meng X., Xie Y. // *Advanced Engineering Materials* . 2019. Vol. 21. 1900343. DOI: 10.1002/ADEM.201900343
6. Gao M.C., Liaw P.K., Yeh J.W., Zhang Y. // *High-Entropy Alloys: Fundamentals and Applications.* 2016. P. 1–516. DOI: 10.1007/978-3-319-27013-5/COVER
7. Gromov V.E., Konovalov S. V., Ivanov Y.F., Osintsev K.A. *Structure and Properties of High-Entropy Alloys.* 2021. Vol. 107. DOI: 10.1007/978-3-030-78364-8
8. Rogachev A.S. // *Physics of Metals and Metallography.* 2020. Vol. 121. P. 733–764. DOI: 10.1134/S0031918X20080098
9. Dewangan S.K., Mangish A., Kumar S., Sharma A., Ahn B., Kumar V. // E *ngineering Science and Technology, an International Journal.* 2022. Vol. 35. P. 101211. DOI: 10.1016/J.JESTCH.2022.101211
10. Wang M., Wen Z., Ma B., Liu J., Zou Z., Zhao Y. // *Journal of Alloys and Compounds.* 2022. Vol. 893. P. 162242. DOI: 10.1016/J.JALLCOM.2021.162242

11. Wu M., Setiawan R.C., Li D.Y. // *Wear.* 2022. Vol. 492–493. P. 204231. DOI: 10.1016/J.WEAR.2021.204231
12. Gao S., Cao J., Qiu Z., Yan X. // *Materials Letters* . 2022. Vol. 321. DOI: 10.1016/J.MATLET.2022.132393
13. Ji F., Wang Z., Wu L. // *Materials Today Communications.* 2022. Vol. 32. P. 104063. DOI: 10.1016/J.MTCOMM.2022.104063
14. Zhang Y., Liu M., Sun J., Li G., Zheng R., Xiao W., et al. // *Materials Science and Engineering: A* . 2022. Vol. 835. P. 142670. DOI: 10.1016/J.MSEA.2022.142670
15. Kumari P., Mishra R.K., Gupta A.K., Mohapatra S., Shahi R.R. // *Journal of Alloys and Compounds* . 2023. Vol. 931. P. 167451. DOI: 10.1016/J.JALLCOM.2022.167451
16. Kitagawa J. // *Journal of Magnetism and Magnetic Materials.* 2022. Vol. 563. P. 170024. DOI: 10.1016/J.JMMM.2022.170024
17. Poliakov M., Kovalev D., Vadchenko S., Moskovskikh D., Kiryukhantsev-Korneev P., Volkova L., et al. // *Nanomaterials.* 2023. Vol. 13. art. no. 2004. DOI: 10.3390/nano13132004
18. Cantor B., Chang I.T.H., Knight P., Vincent A.J.B. // *Materials Science and Engineering: A.* 2004. Vol. 375–377. P. 213–218. DOI: 10.1016/J.MSEA.2003.10.257
19. Xue L., Shao L., Zhang B., Li Z., Cheng J., Shen B. // *Journal of Rare Earths.* 2024. Vol. 42. P. 129–136. DOI: 10.1016/J.JRE.2022.12.001
20. Wang Z., Chen S., Yang S., Luo Q., Jin Y., Xie W., et al. // *Journal of Materials Science & Technology.* 2023. Vol. 151. P. 41–65. DOI: 10.1016/J.JMST.2022.11.054
21. Fan X.J., Qu R.T., Zhang Z.F. // *Journal of Materials Science & Technology* . 2022. Vol. 123. P. 70–77. DOI: 10.1016/J.JMST.2022.01.017

22. Zhu C., Li Z., Hong C., Dai P., Chen J. // *International Journal of Refractory Metals and Hard Materials.* 2020. Vol. 93. DOI: 10.1016/J.IJRMHM.2020.105357
23. Lin M.I., Tsai M.H., Shen W.J., Yeh J.W. // *Thin Solid Films.* 2010. Vol. 518. P. 2732–2737. DOI: 10.1016/J.TSF.2009.10.142
24. Tunes M.A, Fritze S., Osinger B., Willenshofer P., Alvarado A.M., Martinez E., et al. // *Acta Materialia.* 2023. Vol. 250. P. 118856. DOI: 10.1016/j.actamat.2023.118856.
25. Wang B., Wang Q., Sun B., Mo J., Guo Y., Liang X., et al. // *Journal of Materials Science & Technology* . 2023. Vol. 149. P. 31–41. DOI: 10.1016/J.JMST.2022.12.010
26. Dong S., Zhou H., Hu X., Zhang J., Li Y., Shang W., et al. // *International Journal of Hydrogen Energy* . 2023. Vol. 48. P. 18233–18244. DOI: 10.1016/J.IJHYDENE.2023.01.305
27. Gild J., Braun J., Kaufmann K., Marin E., Harrington T., Hopkins P., et al. // *Journal of Materiomics* . 2019. Vol. 5. P. 337–343. DOI: 10.1016/J.JMAT.2019.03.002
28. Yi G., Ding Y., Cheng Y., Zhang P., Wang X., Liang X. // *Journal of Alloys and Compounds.* 2022. Vol. 916. P. 165384. DOI: 10.1016/J.JALLCOM.2022.165384
29. Liu D., Huang Y., Liu L., Zhang L. // *Materials Letters* . 2020. Vol. 268. P. 127629. DOI: 10.1016/J.MATLET.2020.127629
30. Guo Z., Zhang L., Qiao Y., Gao Q., Xiao Z. // *Scripta Materiali* a. 2022. Vol. 218. P. 114798. DOI: 10.1016/J.SCRIPTAMAT.2022.114798
31. Chen Y., Gao X., Qin G., Chen R., Guo J. // *Materials Letters.* 2023. Vol. 335. P. 133832. DOI: 10.1016/J.MATLET.2023.133832
32. Xu Z.Q., Ma Z.L., Tan Y., Wang M., Zhao Y., Cheng X.W. // *Journal of*

Alloys and Compounds. 2022. Vol. 900. P. 163517. DOI: 10.1016/J.JALLCOM.2021.163517

33. Xiao Z., Zhang L., Guo Z. // *Computational Materials Science.* 2022. Vol. 203. P. 111116. DOI: 10.1016/J.COMMATSCI.2021.111116
34. Galetz M.C., Ulrich A.S., Hasemann G., Krüger M. // *Intermetallics.* 2022. Vol. 148. P. 107620. DOI: 10.1016/J.INTERMET.2022.107620
35. Kiryukhantsev-Korneev Ph.V., Chertova A.D., Chudarin F.I., Patsera E.I., Levashov E.A. // *Surface and Coating Technology* . 2024. (in press)
36. Fabrizi A., Cecchini R., Kiryukhantsev-Korneev P. V., Sheveyko A.N., Spigarelli S., Cabibbo M. // *Protection of Metals and Physical Chemistry of Surfaces* . 2017. Vol. 53. P. 452–459. DOI: 10.1134/S2070205117030066
37. Kiryukhantsev-Korneev P. V., Andreev S.O., Shvyndina N. V., Levashov E.A., Timofeev A.N., Shtansky D. V. // *Russian Journal of Non-Ferrous Metals.* 2014. Vol. 55. P. 645–651. DOI: 10.3103/S106782121406011X
38. Kiryukhantsev-Korneev P., Sytchenko A., Pogozhev Y., Vorotilo S., Orekhov A., Loginov P., et al. // *Materials* . 2021. Vol. 14. DOI: 10.3390/MA14081932
39. Yao X.Y., Li H.J., Zhang Y.L., Ren J.J., Yao D.J., Tao J. // *Corrosion Science* . 2012. Vol. 57. P. 148–153. DOI: 10.1016/J.CORSCI.2011.12.023
40. Bae K.E., Chae K.W., Park J.K., Lee W.S., Baik Y.J. // *Surface and Coatings Technology.* 2015. Vol. 276. P. 55–58. DOI: 10.1016/J.SURFCOAT.2015.06.053
41. Kiryukhantsev-Korneev F. V., Lemesheva M. V., Shvyndina N. V., Levashov E.A., Potanin A.Y. // *Protection of Metals and Physical Chemistry of Surfaces* . 2018. Vol. 54. P. 1147–1156. DOI: 10.1134/S207020511806014X/FIGURES/10
42. Kiryukhantsev-Korneev P. V., Potanin A.Y. // *Russian Journal of Non-*

Ferrous Metals. 2019. Vol. 59. P. 698–708. DOI: 10.3103/S106782121806010X

43. Kiryukhantsev-Korneev P. V., Kuptsov K.A., Tabachkova N.Y., Andreev N. V., Sagalova T.B., Golizadeh M., et al. // *Protection of Metals and Physical Chemistry of Surfaces.* 2021. Vol. 57. P. 1008–1024. DOI: 10.1134/S2070205121050130/FIGURES/11
44. Kiryukhantsev-Korneev P. V., Sheveyko A.N., Levashov E.A., Shtansky D. V. // *Russian Journal of Non-Ferrous Metals* . 2015. Vol. 56. P. 540–547. DOI: 10.3103/S1067821215050077/METRICS
45. Kiryukhantsev-Korneev P. V., Sytchenko A.D., Sviridova T.A., Sidorenko D.A., Andreev N. V., Klechkovskaya V. V., et al. // *Surface and Coatings Technology.* 2022. P. 128141. DOI: 10.1016/J.SURFCOAT.2022.128141
46. Kiryukhantsev-Korneev Ph.V. // *Protection of Metals and Physical Chemistry of Surfaces.* 2012. Vol. 48. P. 585 - 590. DOI: 10.1134/S207020511205005X
47. Lange A., Braun R., Heilmaier M. // *Intermetallics.* 2014. Vol. 48. P. 19–27. DOI: 10.1016/J.INTERMET.2013.09.007
48. Choi Y.J., Yoon J.K., Kim G.H., Yoon W.Y., Doh J.M., Hong K.T. // *Corrosion Science.* 2017. Vol. 129. P. 102–114. DOI: 10.1016/J.CORSCI.2017.10.002
49. Asempah I., Xu J., Yu L., Wang L. // *Ceramics International.* 2019. Vol. 45. P. 19395–19403. DOI: 10.1016/J.CERAMINT.2019.06.192
50. Xie Z.W., Wang L.P., Wang X.F., Huang L., Lu Y., Yan J.C. // *Transactions of Nonferrous Metals Society of China (English Edition)* . 2011. Vol. 21. DOI: 10.1016/S1003-6326(11)61628-2
51. Shi X., Zhao Y., Gao X., Li J., Chen J., You Y., et al. // *Ceramics International.* 2024. Vol. 50. P. 1166–1178. DOI: 10.1016/J.CERAMINT.2023.10.209

52. Lapshin O. V., Boldyreva E. V., Boldyrev V. V. // *Russian Journal of Inorganic Chemistry.* 2021. Vol. 66. P. 433–453. DOI: 10.1134/S0036023621030116
53. Kovalev D.Y., Potanin A.Y., Levashov E.A., Shkodich N.F. // *Ceramics International* . 2016. Vol. 42. P. 2951–2959. DOI: 10.1016/J.CERAMINT.2015.10.078
54. Rakhadilov B., Kakimzhanov D., Buitkenov D., Abdulina S., Zhurerova L., Sagdoldina Z. // *Crystals.* 2022, Vol 12, Page 1388. DOI: 10.3390/CRYST12101388
55. Golizadeh M., Kuptsov K.A., Shvyndina N. V., Shtansky D. V. // *Surface and Coatings Technology.* 2017. Vol. 319. P. 277–285. DOI: 10.1016/J.SURFCOAT.2017.04.016

Figure Captions

Figure 1 – SEM micrographs of fracture surfaces of coatings SL (a), DL (b), ML (c), NC (d). X-ray diffraction patterns of coatings (e).

Figure 2 – Elemental OESTR profiles of coatings SL (a), DL (b), ML (c), NC (d)

Figure 3 – Dependence of Δm/S on holding time (a) and appearance (b) of coatings during annealing at a temperature of 1000 °C and holding times from 0 to 180 min

Figure 4 – SEM micrographs of the surface of coatings SL (a), DL (b), ML (c), NC (d) after annealing at a temperature of 1500 °C with a holding time of 10 min

Figure 5 – SEM images of cross-sectional fractures and EDS maps for coatings SL (a), DL (b), ML (c), NC (d) after annealing at a temperature of 1500 °C

Figure 6 – Thickness of the oxidized layer (h_{ox}) and the difference between the thickness of the initial coating and the thickness of the non-oxidized layer after annealing (a) and specific mass change (Δm/S) (b) at a temperature of 1500 °C ($h_{init} - h_{non\text{-}ox}$) for coatings SL, DL, ML, NC

Figure 7 – SEM micrographs of the surface of coatings SL (a), DL (b), ML (c), NC (d) after annealing at a temperature of 1500 °C with a holding time of 10 min

Figure 8 – SEM images of cross-sectional fractures and EDS maps for coatings SL (a), DL (b), ML (c), NC (d) after annealing at a temperature of 1600 °C

Figure 9 – X-ray diffraction patterns of coatings after annealing at 1500 (a) and 1600 °C (b)

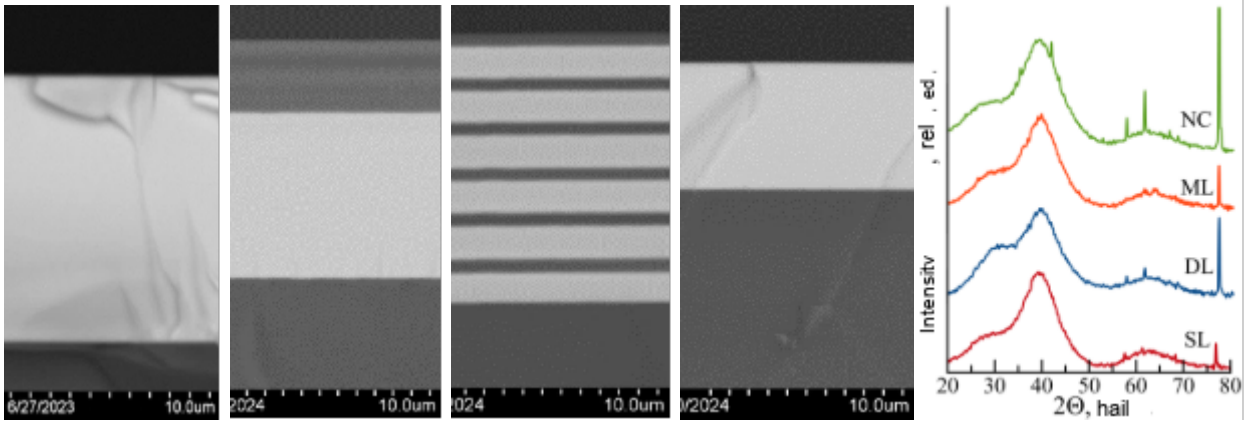

Figure 1

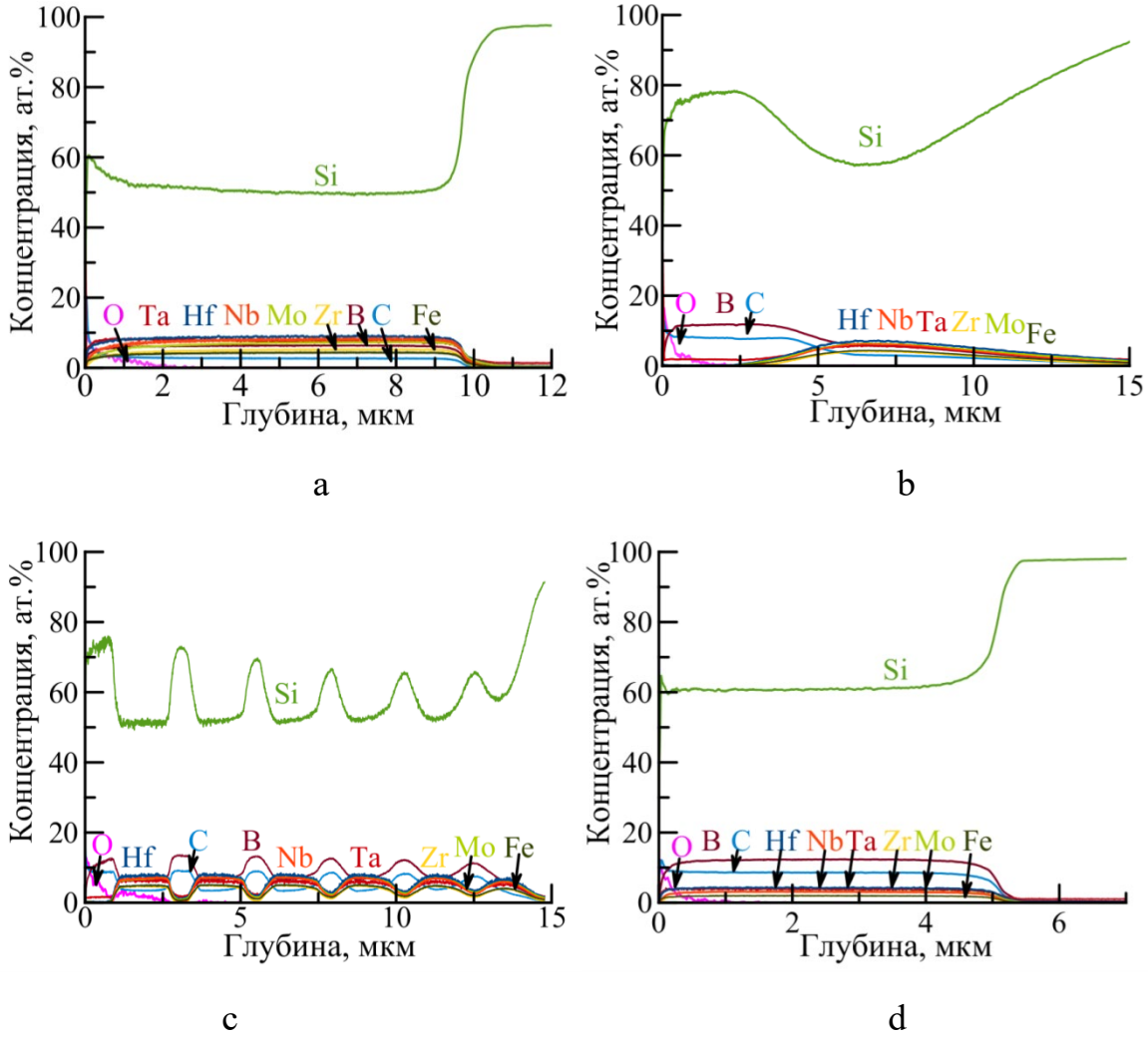
Концентрация, ат.%
Глубина, мкм
Si
O Ta Hf Nb Mo Zr B C Fe
a
Si
O B C
Hf Nb Ta Zr Mo Fe
b
Si
O Hf C B Nb Ta Zr Mo Fe
c
Si
O B C Hf Nb Ta Zr Mo Fe
d

Figure 2

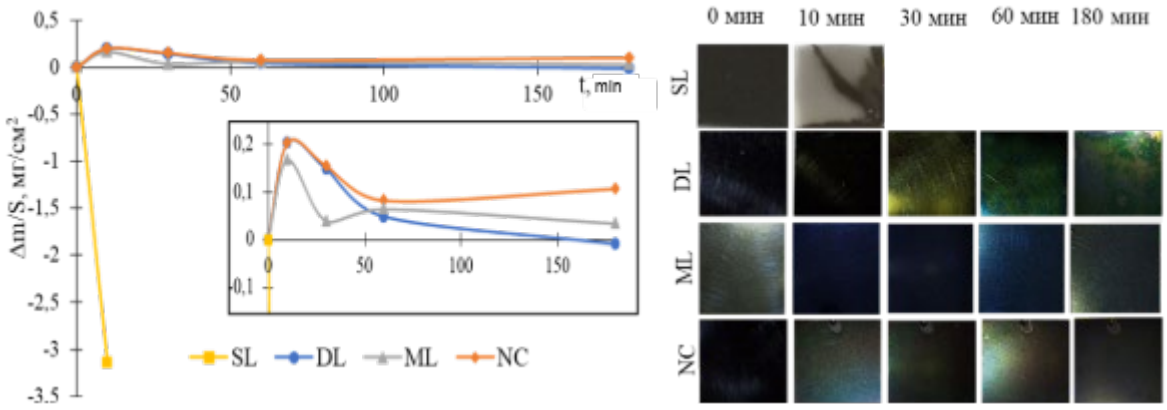

a b

Figure 3

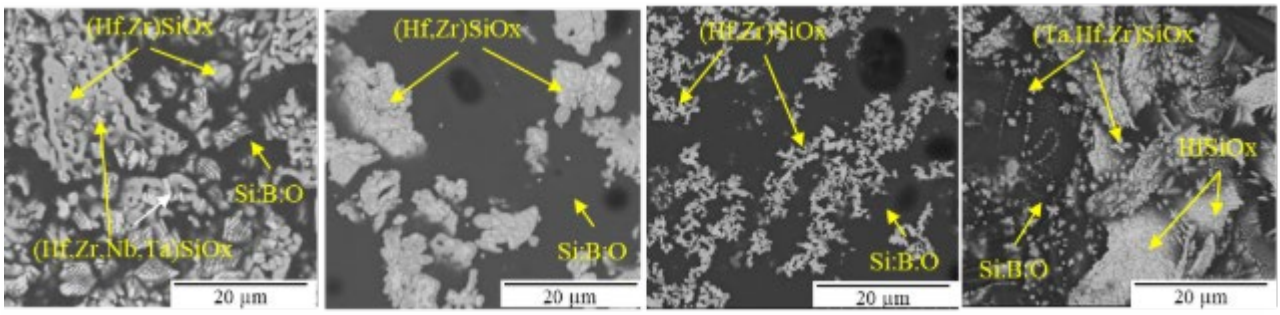

a b c d

Figure 4

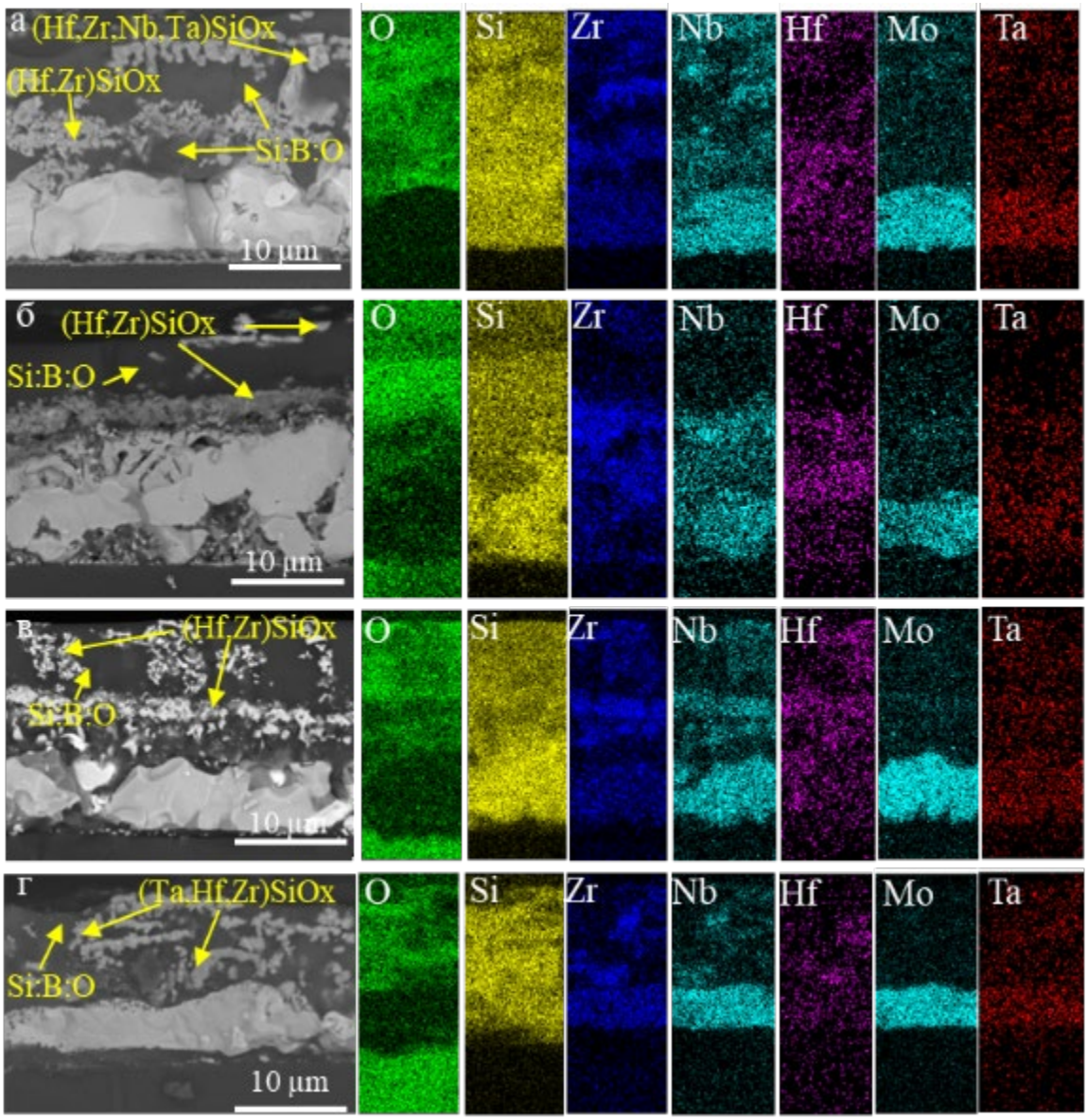
а
(Hf,Zr,Nb,Ta)SiOx
(Hf,Zr)SiOx
Si:B:O
10 μm
O
Si
Zr
Nb
Hf
Mo
Ta
б
(Hf,Zr)SiOx
Si:B:O
10 μm
O
Si
Zr
Nb
Hf
Mo
Ta
в
(Hf,Zr)SiOx
Si:B:O
10 μm
O
Si
Zr
Nb
Hf
Mo
Ta
г
(Ta,Hf,Zr)SiOx
Si:B:O
10 μm
O
Si
Zr
Nb
Hf
Mo
Ta

Figure 5

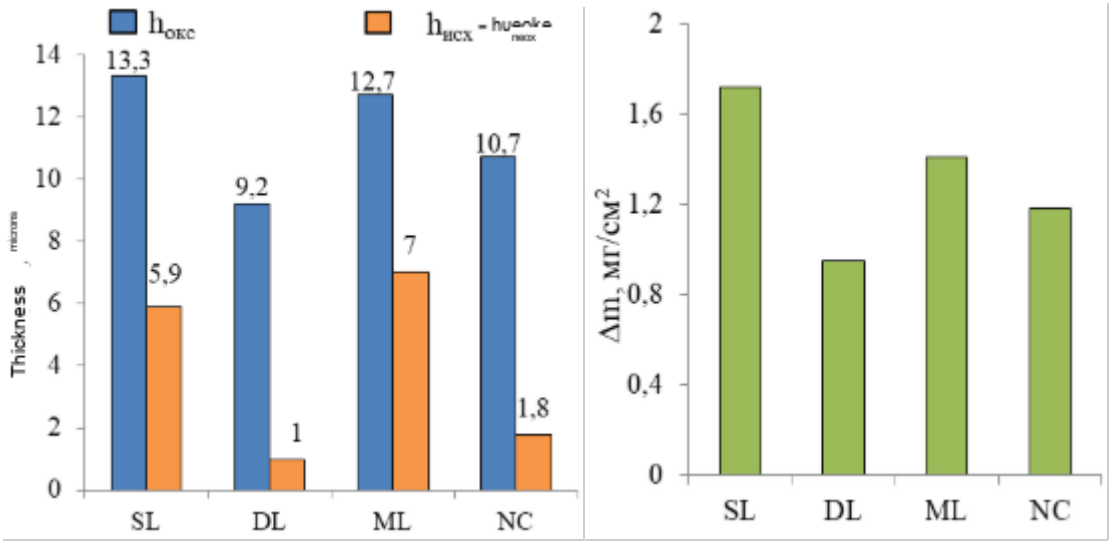

a b

Figure 6

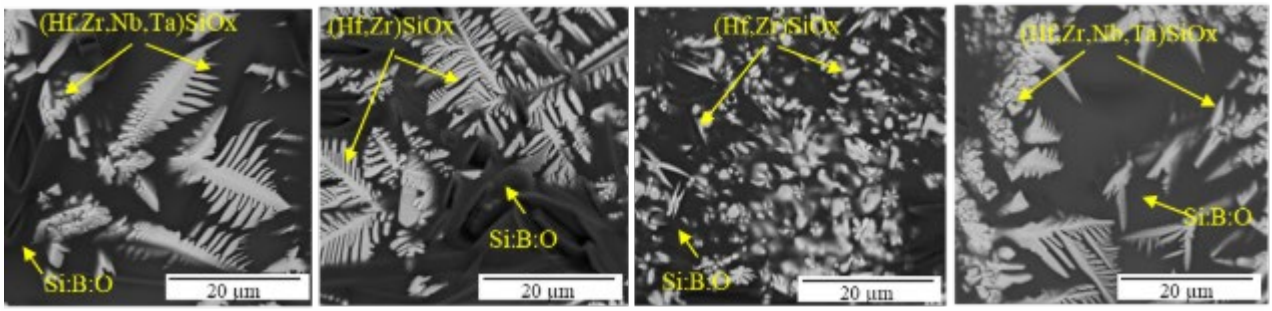

a b c d

Figure 7

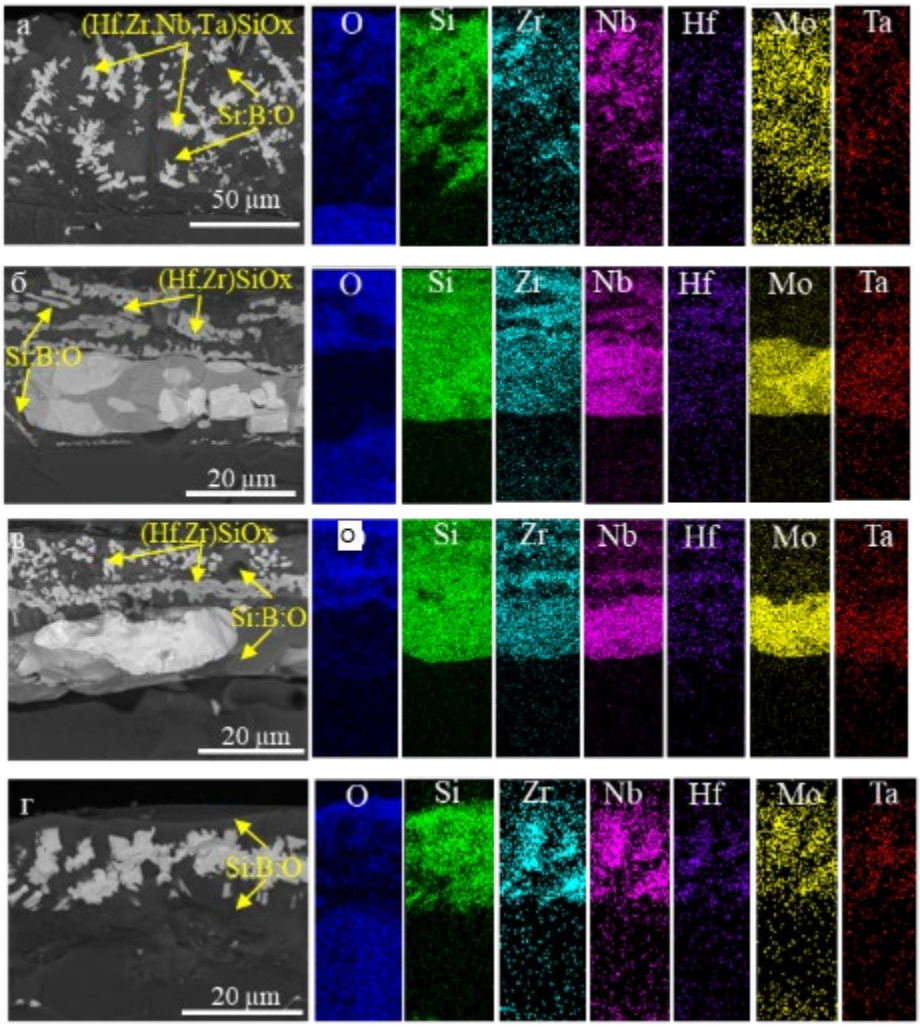
а
(Hf,Zr,Nb,Ta)SiOx
Si:B:O
50 μm
O
Si
Zr
Nb
Hf
Mo
Ta
б
(Hf,Zr)SiOx
Si:B:O
20 μm
в
(Hf,Zr)SiOx
Si:B:O
20 μm
г
Si:B:O
20 μm

Figure 8

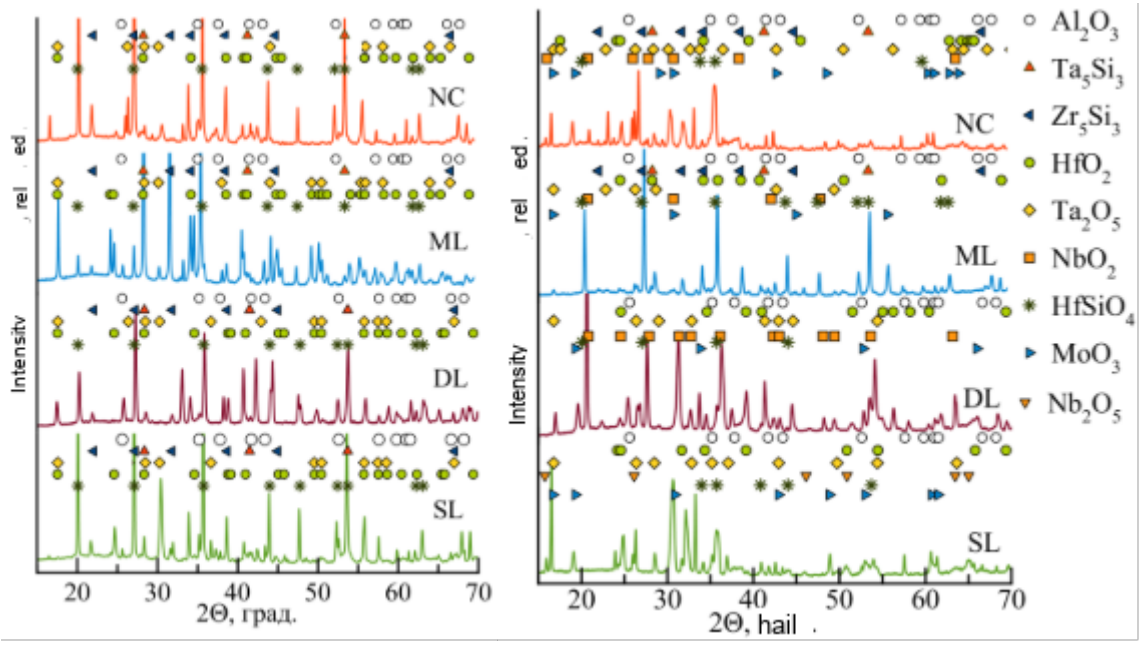
NC
ML
DL
SL
Intensity
2Θ, град.
2Θ, hail
Al2O3
Ta5Si3
Zr5Si3
HfO2
Ta2O5
NbO2
HfSiO4
MoO3
Nb2O5

a b

Figure 9